Chapter 1
Holographic Liquid Crystals
for Nanophotonics

Timothy D. Wilkinson, Haider Butt and Yunuen Montelongo

Abstract Nanotechnology offers a new paradigm in ways of controlling light in optical systems. Optically enhanced effects such plasmonic resonances and nano-antennas combined with diffraction and photonic bandgap effects can create new mechanisms to enhance the performance of modulation technologies in applications such as three dimensional displays. The power of these optical effects can then be made even more effective by adding in a variable refractive index material such a liquid crystal. This allows the optical properties to be tuned or modulated and creates a new class of optical devices which utilise features on the nano-scale. This chapter pulls together the various strands that have been developed in this area to make an initial investigation into these types of devices. The power of diffraction is introduced to propagate light in a manner which ideally suits nanotechnology. This is then combined with the algorithms used to create computer generated holograms to demonstrate that the diffraction process is indeed the key to the optical control mechanisms at length scales of the order of the wavelength of the light. The key properties of carbon nanotubes and liquid crystals are then introduced to provide the means to create enhanced diffraction through resonant effects which can then be tuned through the variable refractive index properties of the liquid crystals. The most important property of the nanotechnology is the ability to have electrically conductive structures on the nanometre length scale, which allows the rules of electric field interaction to ne manipulated by plasmonics. These effects are demonstrated using both conducting multiwall carbon nanotubes as well as silver nano-antennas. Plasmonic resonance in arrays of nanotubes show the predicted wavelength cut off due to a negative dielectric constant. The same effects are then linked with diffraction to create quasi-crystalline diffraction patterns and fully

T. D. Wilkinson (✉) · Y. Montelongo
Electrical Engineering Division, University of Cambridge, Cambridge, UK
e-mail: tdw13@cam.ac.uk

H. Butt
School of Mechanical Engineering, University of Birmingham, Birmingham B15 2TT, Edgbaston, UK
e-mail: h.butt@bham.ac.uk

synthetic computer generated holograms. These effects are expanded further with the silver nano-antennas, where the enhanced resonance effects allow the control of polarisation as well as the wavefront through diffraction. Finally the liquid crystal element of variable refractive index is added to the devices to control the resonance and tune its performance. While this is still at a very early stage of research, it already demonstrates the power and versatility created by the combination of these different optical effects.

1.1 Introduction

Computer generated holography has a very long and distinguished career in the world of photonic research [1–5], however it has never quite lived up to its potential due to the limitations of the technology chosen to display the holograms. Classical photographic film holograms as pioneered by Gabor [6, 7] and later Leith [8], demonstrate the true potential of holograms for the display of three dimensional (3D) images, however research has yet to come up with a truly reconfigurable version that would allow computer generated holograms (CGHs) to live up to their true potential. Recent work has demonstrated reconfigurable holograms for 3D display based on photo-addressed polymer materials [9], but the technique is still limited by the need for an optical assembly to allow the interference patterns to be recorded. The sort of modulation that is required to replicate these holograms is highly complex in nature, very high resolution and uses sub-wavelength pitch pixels. The challenge is to find a dynamically addressed technology that can in some way come close to the sort of modulation that has been achieved with optically recorded interference patterns.

The power of the CGH is that the hologram can be calculated offline and then stored for later display, or can be calculated in real time using an appropriate algorithm. Once the CGH has been calculated, the next stage is then to match the hologram to the desired modulation technology. Liquid crystals (LCs) offer a tantalizingly close approximation to the sort of refractive index change seen in photographically reordered holograms, only with a much reduced resolution and larger pixel size. The holograms written in [4] show that LCs can get close to the sort of resolutions desired in these holograms and recent advances in ultra high-definition displays show that it is possible to electrically address the huge amount of information contained within these holograms. The final hurdle is to reduce the pixel pitch in these LC devices to get to the order or even better below the wavelength of the light used to illuminate the hologram. This is still a very significant challenge, however nano-photonic devices are beginning to hint at the potential for this technology. Materials such as multi-walled carbon nanotubes (MWCNTs) off the possibility of integrating sub-wavelength structures which can be sued to electrically control the LC director [10]. These materials are also demonstrating enhanced electronic properties such as plasmonic resonances [11] which further enhance their optical properties and expand the potential of their use

in holography. In this chapter we explore the potential of these structures and where applicable their interaction with LCs in order to make the first steps towards a truly electrically reconfigurable holographic structure.

1.2 Computer Generated Holography

1.2.1 Diffraction Through an Aperture

In order to understand how nano technology can be used in computer generated holography, we need understand the basics of diffraction theory. This is covered in much better detail in several fundamental texts [12, 13], so we will only summarise the key aspects in this chapter. Let us assume we have an arbitrary aperture (hole) function, $A(x, y)$ in the plane S as shown in Fig. 1.1, with coordinates [x, y]. The light passing through this aperture will be diffracted at its edges and the exact form of this pattern can be calculated. We want to calculate the field distribution at an arbitrary position away at the point P, which is a distance R from the aperture.

If we consider an infinitely small differential of the aperture, dS, we can model this as a point source of light emitting spherical 'Huygens' wavelets with an amplitude of $A(x, y)dS$. The wavelet acts as a radiating point source, so we can calculate its field at the point P, a distance r from dS. The point source dS can be considered to radiate a spherical wave front of frequency ω. The total field distribution at P is evaluated by superposition (summation) of all the wavelets across the aperture. The process of interference of these spherical wavelets is called diffraction and is based on the Huygens-Fresnel approximation. In order to understand and analyse the propagating wavelets, a series of approximations and assumptions must be made. If we consider only the part of the wavelets which are propagating in the forward ($+z$) direction and are contained in a cone of small angles away from the z axis, then we can evaluate the change in field dE at the point P, due to dS. As the wavelet dS acts as a point source, we can say that the power radiated is proportional to $1/r^2$ (spherical wavefront), hence the field dE will be proportional to $1/r$. We can see that for a real propagating wave of frequency ω and wave number k, ($k = 2\pi/\lambda$) we have at point P,

$$dE = \frac{A(x, y)}{r} e^{jwt} e^{-jkr} dS. \tag{1.1}$$

Now, we need to change coordinates to the plane containing the point P, which are defined as [α, β] to give the full expression for each wavelet in terms of x and y ($dS = dxdy$) for dE will now be.

$$dE = \frac{A(x, y)e^{j\omega t} e^{-jkR\sqrt{1 - \frac{2\alpha x + 2\beta y}{R^2} + \frac{x^2 + y^2}{R^2}}}}{R\sqrt{1 - \frac{2\alpha x + 2\beta y}{R^2} + \frac{x^2 + y^2}{R^2}}} dxdy. \tag{1.2}$$
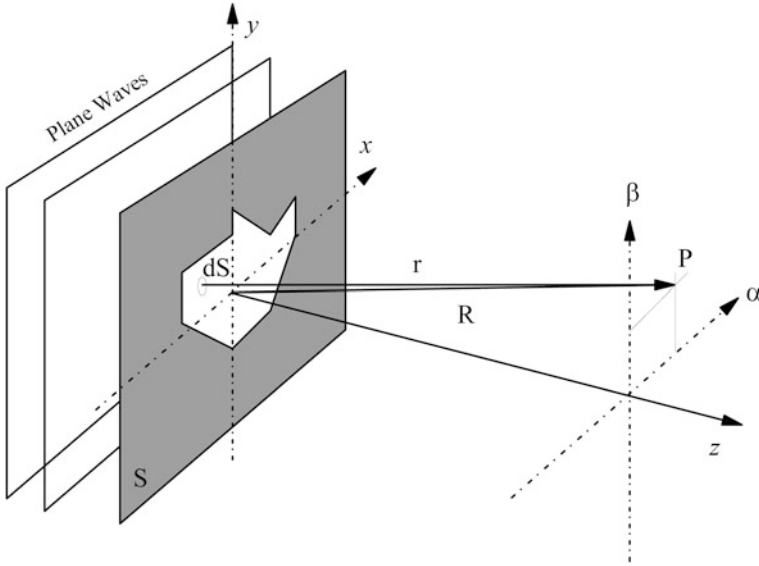
Fig. 1.1 Aperture and diffraction coordinate system

Such an expression can only be solved directly for a few specific aperture functions. To account for an arbitrary aperture, we must approximate, simplify and restrict the regions in which we evaluate the diffracted pattern. If the point P is reasonably coaxial (close to the z axis, relative to the distance R) and the aperture $A(x, y)$ is small compared to the distance R, then the lower section of (1.2) for dE can be assumed to be almost constant and that for all intents and purposes, $r = R$. The similar expression in the exponential term in the top line of (1.2) is not so simple. It cannot be considered constant as small variations are amplified through the exponential. To simplify this section we must consider only the far field or Fraunhofer region where,

$$R^2 \gg x^2 + y^2. \tag{1.3}$$

In this case, the final term in the exponential can be considered negligible. To further simplify, we use the binomial expansion, and keep the first two terms only to further simplify the exponential expression. Hence the simplified version of the field dE, can be expressed as,

$$dE = \frac{A(x, y)}{R} e^{j(\omega t - kr)} e^{jk\left(\frac{\alpha x + \beta y}{R}\right)} dx dy. \tag{1.4}$$

The regions of the approximation are defined such that in the far field or Fraunhofer region, the approximations are accurate, hence the field distribution $E(x, y)$ only changes in size with increasing z, rather than changes in structure as demonstrated in Fig. 1.2. In the case where the approximation is bearably accurate,
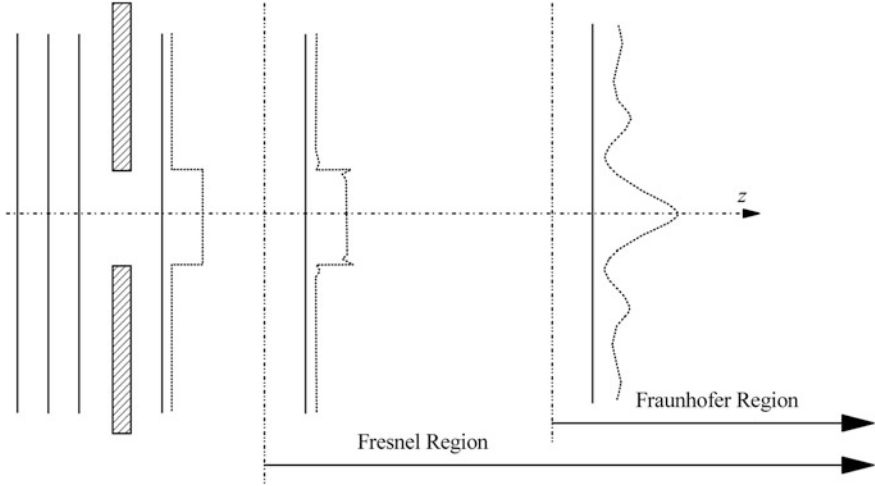
Fig. 1.2 Diffraction regions for a square aperture

we are in the Fresnel region. Before the Fresnel region, the evaluation of E is extremely difficult and is defined as the near field diffraction pattern. The exact boundary of the Fresnel region will depend on the acceptable accuracy and can be found in Goodman [12].

The total effect of the dS wavelets can be integrated across dE to get an expression for the far field or Fraunhofer diffraction pattern. The initial exponential term $e^{j(\omega t - kR)}$ in (1.4) refers the wave to an origin at $t = 0$, but we are only interested in the scaling of relative points at P with respect to each other, so it is safe to normalise this term to unity. Thus, our final expression for the far field diffraction pattern becomes,

$$E(\alpha, \beta) = \iint\limits_{A} A(x, y) e^{jk(\alpha x + \beta y)/R} dxdy. \tag{1.5}$$

Hence the far field diffraction pattern at the point P is related to the aperture function $A(x, y)$, by the Fourier transform. The final step is to remove the scaling effect of R in the equation, as it does not affect its structure, just its size. The coordinates $[\alpha, \beta]$ are absolute and are scaled by the factor R. For this reason, we normalise the coordinates and define the Fourier transform of the aperture in terms of its spatial frequency components $[u, v]$,

$$u = \frac{k\alpha}{2\pi R} \quad \text{and} \quad v = \frac{k\beta}{2\pi R}, \tag{1.6}$$

and the final relationship is,

$$E(u, v) = \iint\limits_{A} A(x, y)e^{2\pi j(ux+vy)}dxdy. \tag{1.7}$$

And inversely we can calculate the aperture from the far field pattern.

$$A(x, y) = \iint\limits_{A} E(u, v)e^{-2\pi j(ux+vy)}dudv. \tag{1.8}$$

This relationship also gives us the scaling law for computer generated holograms. As an example, the far field pattern of a square aperture of width 1 mm, at a wavelength of 633 nm can only be accurately measured 10 m away from the aperture. Such a far field distance is clearly difficult to achieve in practical terms, hence either smaller apertures are required, or a positive focal length lens can be included directly after the aperture to create the far field of the aperture in the focal plane of the lens [12]. A positive lens performs a Fourier transform of the aperture placed behind it. The final result for the diffracted aperture $A(x, y)$ a distance d behind a positive focal length lens of focal length f, given by,

$$E(\alpha, \beta) = e^{\frac{jk}{2f}\left(1-\frac{d}{f}\right)\left(\alpha^2+\beta^2\right)} \iint\limits_{A} A(x, y)e^{\frac{jk}{f}(\alpha x+\beta y)}dxdy. \tag{1.9}$$

Once again we can translate the equation into spatial coordinates such that now the scaling coordinates are,

$$u = \frac{k\alpha}{2\pi f} \quad \text{and} \quad v = \frac{k\beta}{2\pi f}. \tag{1.10}$$

We want to calculate the far field or Fraunhofer region for a square aperture. This aperture can be represented in one dimension as a rectangular or 'Rect' function. Hence the Fourier transform of this will be a one dimensional sinc function, where $sinc(x) = sin(x)/x$. The sinc finction is shown in Fig. 1.3 and is one of the fundamental structures that dominates the information generated by computer generated holograms

It is simple to repeat this calculation in the orthogonal direction to create the far field diffraction pattern in two dimensions. The far field of a square aperture with transmission of A and width a therefore its Fourier transform,

$$F(u, v) = Aa^2 sinc(\pi au)sinc(\pi av). \tag{1.11}$$

The resulting two dimensional sinc function has a very strong effect on the structure of the replay field of a hologram as it forms the overall envelope that will contain the desired information as well as having repeating sidelobes that represent the higher order diffraction terms as shown in Fig. 1.3. Now we will look at what

Fig. 1.3 The one dimensional sinc function (sinc envelope)
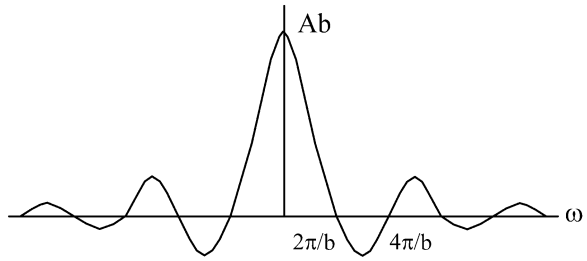
happens when we shift the aperture by a distance $a/2$ from the origin of the plane using the shift theorem for Fourier transforms.

$$F(u, v) = Aa^2 e^{j\pi au} \text{sinc}(\pi au) \text{sinc}(\pi av). \tag{1.12}$$

The result in (1.12) is same sinc function as (1.11), but with an additional phase term due to the shift. By combining an array of these apertures (now referred to as pixels) at various positions on a regular sampled grid, it is possible to generate a complex amplitude function in the far field. Such a two dimensional (2D) combination of these pixels in various positions is defined as a Hologram and the pattern generated by the hologram if the far field is the Replay Field. Hence a hologram can be designed by selecting the positions of the apertures that will combine together through diffraction to generate the desired optical intensity in the replay field. By altering the value of the transmitted amplitude A of each pixel, centred on a grid of interval a (note that the sampling grid does not have to equal the size of the aperture), it is possible to add up the 2D sinc functions and create an arbitrary 2D distribution in the far field region. By superimposing all the exponential phase terms due to the shift and varying the amplitude A, it is possible to create useful patterns in the far field. In general terms, the broader the feature or combination of pixels, the smaller or more delta function-like the replay object. Also, repetitive pixel patterns in the hologram leads to repetitive features in the replay field.

The exact structure of the replay field distribution depends on the shape of the "fundamental" pixel and the number and distribution of these pixels in the hologram. The pattern we generate with this distribution of pixels is repeated in each lobe of the sinc function from the fundamental pixel. The lobes can be considered as spatial harmonics of the central lobe, which contains the desired 2D pattern. For example, a line of square pixels with alternate pixels being one or zero (i.e. a square wave) would have the basic replay structure seen in Fig. 1.4.

There is a direct analogy between the one dimensional (1D) and 2D examples. The repetition of a square wave leads to discrete sampling in the frequency domain. In the case of the square wave, there is a series of odd harmonics generated. In 2D, these harmonics appear as orders radiating out in the lobes of the sinc function from the dimensions of the fundamental aperture or pixel. The more pixels we have in the hologram, the closer we get to the infinite case and spots generated become more like delta functions.

Fig. 1.4 Fourier transform of a square wave (50/50 mark space ratio)
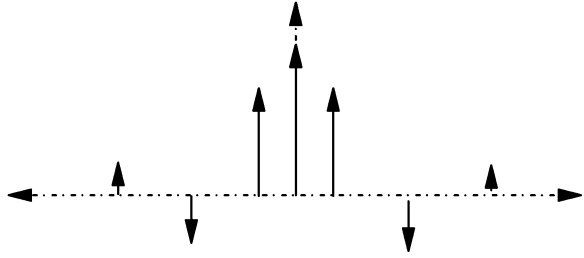
So far we have assumed that the aperture A can only modulate intensity or amplitude between pixels. There is a limitation if we have binary amplitude modulation $A \in [0, 1]$ which is that the central point at the origin (defined as the zero order) of the replay field can only be zero if all values of A are zero. This is because the point at the origin of the replay field is proportional to the average of the pixels in the grating or hologram. A better modulation scheme would be binary phase modulation where $A \in [+1, -1]$. If there are the same number of pixels set to $+1$ as set to -1, then the average will be zero and the zero order will be zero too. A simple proof of this is as follows. Hence, with binary phase modulation ($A \in [+1, -1]$), the pixel in the centre of the replay field can be defined by the structure of the hologram. A drawback of both these binary modulation schemes is that the hologram will always be a real function.

$$F_T[h(x, y)^*] = H(-u, -v). \tag{1.13}$$

If function $h(x, y)$ is real then $h(x, y)^* = h(x, y)$, hence we cannot differentiate between $H(u, v)$ and $H(-u, -v)$ which means that both must appear in the replay field. Hence any replay field generated by a binary phase or amplitude hologram will always have $180°$ rotational symmetry. This symmetry restricts the useful area of the replay field to the upper half plane of the sinc envelope, as any pattern generated by the hologram will automatically appear as desired as well as rotated about the origin by $180°$.

The next step is to look at 2D patterns such as the chequerboard pattern in Fig. 1.5, of pixels on an equally spaced grid (for simplicity A is restricted to binary values (such as 0 or 1). The chequerboard can be generated by the XOR of a 2D grating with itself rotated by $180°$. Hence, the replay field will be made from the convolution of the FT of the two gratings.

1.2.2 Calculating Computer Generated Holograms

There is no simple way of generating a hologram analytically except for general cases such as gratings [14] and chequerboards. In order to create a hologram which generates an arbitrary replay field we need a more sophisticated algorithm. In order
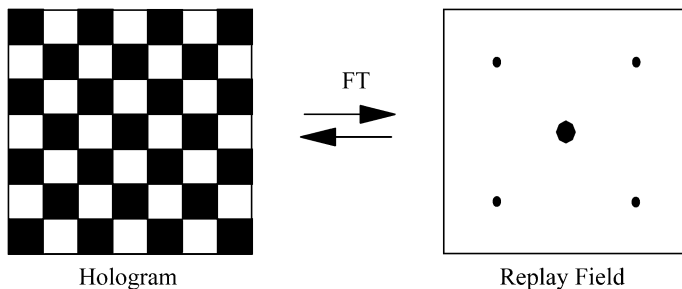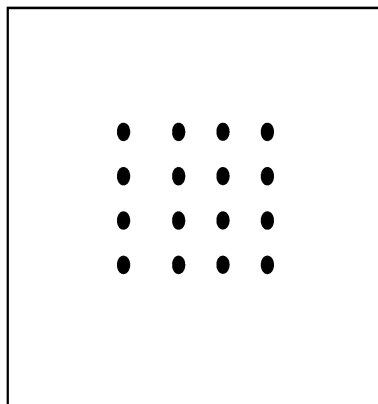
Fig. 1.5 Chequerboard hologram and its far field diffraction pattern

Fig. 1.6 Target function of
4×4 spots (on a 64×64
grid)

to achieve this we must use optimisation techniques such as simulated annealing [15], Gerchberg-Saxon [16] or the genetic algorithm [17]. To illustrate the basic concept of these algorithms we shall look at a simple binary phase only computer generated hologram (CGH) example based on direct binary search, which is a simplification of simulated annealing. Say we want an array of 4×4 delta functions in a square grid spaced as seen in Fig. 1.6.

If we take the FT of the target replay field of Fig. 1.7, then take the phase and threshold it about $\pi/2$ to create a binary hologram as shown in the left side of Fig. 1.7.

The "hologram" and replay field in Fig. 1.8 are clearly not what we desire. Hence we need a better way of finding the optimum combination of pixels to give us the target replay field we desire. The simplest method of generating a CGH, avoiding the problems of Fig. 1.8, is direct binary search (DBS). In this technique we take a hologram of random pixel values and then calculate its replay field. We then flip the binary value of a randomly positioned pixel and calculate the new replay field. We then subtract the two replay fields from the target replay field, sum up the differences to form a cost function for the hologram before and after the pixel change. If the cost function after the pixel has been flipped is less than the
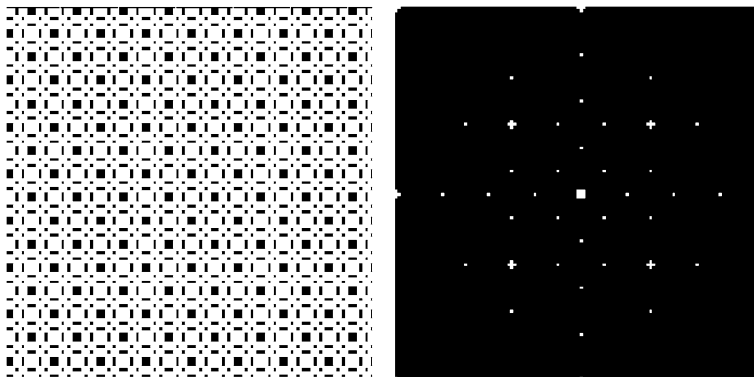
Fig. 1.7 CGH generated by thresholding the phase of FT (target). *Left*, binary phase hologram, right is the replay field generated from it
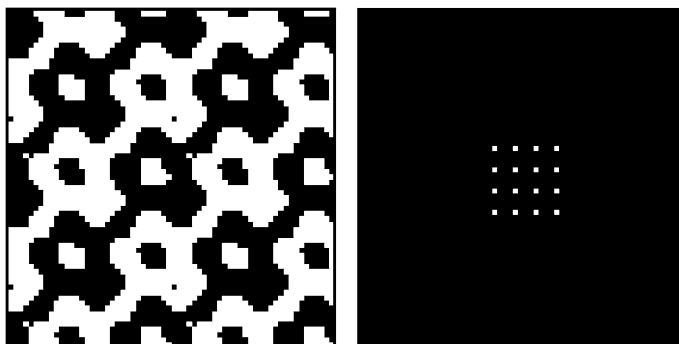

Fig. 1.8 Hologram generated by DBS (*left*) and its replay field (*right*)

cost function before the pixel was flipped, then the pixel change is considered to be advantageous and is accepted. The new cost function is then used in comparison to another randomly chosen flipped pixel. The process repeats until no further pixels can be flipped to give an improvement in the cost function.

Direct Binary Search

(1) Define an ideal target replay field, T (desired pattern as in Fig. 1.6).
(2) Start with a random array of binary phase pixels.
(3) Calculate its replay field (FT), H_0.
(4) Take the difference between T and H_0 and then sum up to make the first cost, C_0.
(5) Flip a pixel state in a random position.
(6) Calculate the new replay field, H_1.

(7) Take the difference between T and H_1 then sum up to make the second cost, C_1.

(8) If $C_0 < C_1$ then reject the pixel flip and flip it back.

(9) If $C_0 > C_1$ then accept the pixel flip and update the cost C_0 with the new cost C_1.

(10) Repeat steps 4–9 until $|C_0 - C_1|$ reaches a minimum value.

This is not a fully optimum means of generating a hologram, but it gives a very good approximation as demonstrated by Fig. 1.8. More sophisticated techniques are required to fully exploit the possible combinations of pixel values in the hologram. One such algorithm is simulated annealing, which uses DBS, but also includes a probabilistic evaluation of the cost function, which changes as the number of iterations increases. The idea is to allow the hologram to "float" during the initial iteration, with good and bad pixel flips being accepted. This lets the optimisation float into a more global minima rather than getting stuck in a local minima as is the case with DBS.

1.3 Carbon Nanotubes

Carbon is the most versatile element in the periodic table because of the different arrangements of electrons around the nucleus of the atom and hence the number of bonds it can form with other elements. There exists three allotropic forms of carbon; graphite, diamond and buckminsterfullerene. Graphite consists of layered planar sheets of sp^2 hybridized carbon atoms bonded together in a hexagonal network. Diamond has a crystalline structure where each sp^3 hybridized carbon atom is bonded to four others in a tetrahedral arrangement. The third allotrope buckminsterfullerene or fullerene (C_{60}) is made up of spheroidal or cylindrical molecules with all the carbon atoms sp^2 hybridize. Smalley [18] proposed the existence of a tubular form of fullerene termed a carbon nanotube (CNT). The experimental evidence of the existence of carbon nanotubes was discovered by Iijima [19] by imaging multi-walled CNTs using transmission electron microscopy. Iijima discovered single walled carbon nanotubes as well 2 years later. A single walled carbon nanotube can be considered as a rolled graphene sheet. CNTs are one of the more promising materials for device fabrication because of their excellent electrical, thermal and mechanical properties in addition to high aspect ratio and high resistance to chemical and physical attack.

CNTs are metallic or semiconducting based on the exact way the CNTs are wrapped. Multi-walled CNTs are metallic in most cases as there are so many layers and the probability is very high of having one wrapped layer in the group to being metallic.

CNTs find applications in the areas such as micro electronics, field emission displays, X-ray sources and gas sensors. Single walled and multi-walled CNTs can be grown using high pressure arcs, laser ablation and chemical vapour deposition.

It is essential to develop a process which enables high yield, high uniformly perfectly aligned nanotubes at precise locations on the substrate in order to utilize their unique properties. The plasma enhanced chemical vapor deposition (PECVD) technique was used to grow uniform, perfectly aligned nanotubes on a Si substrate [20]. The process of using PECVD along with lithographic patterning without the deposition of amorphous carbon (a-C) has been largely ignored in the literature but this work showed the impact of the C_2H_2: NH_3 ratio in the growth of the carbon nanotubes and a-C deposition in the conventional PECVD technique. The plasma is not necessary for the nucleation and growth of nanotubes, but the electric field induced by the plasma is required for the alignment of the nanotubes. The C_2H_2 provides carbon for the growth of the nanotubes, while the NH_3 etches the carbon and hence a balance between the growth of the tubes and removal of a-C is achieved. The C_2H_2: NH_3 ratio was varied from 15 to 75 % in order to investigate the influence of the gas composition on the formation of a-C. The chemical composition of the unpatterned Si areas was investigated by Auger electron spectroscopy (using an in situ 2 keV Ar-ion gun). When the C_2H_2 ratio increased beyond 30 %, a-C deposition also increased and they found a peak when it crossed 50 %. An interface region of Si, C, N_2 and O_2 formed for all C_2H_2 concentrations. It was found that the optimal C_2H_2 ratio for clean nanotubes deposition lies between 15 and 30 %. The thickness of the Ni thin film catalyst controls the diameter, height and density of the nanotubes. The spacing between the nanotubes can be controlled via lithography and the height of the nanotubes by the deposition time of the tip growth mechanism. This pattern and growth method was used for growing uniform patterned multi-walled nanotubes in the nanophotonic devices.

Where V the voltage is applied across the electrodes and d is the gap spacing between the electrodes. If one of the electrodes is replaced by a sharp protrusion or a carbon nanotube, then d is interpreted as the minimum distance between the electrodes. So the local field (within 1–2 nm of the surface atoms) is much higher than the applied field. So the field is very high close to the tip and causes field emission of electrons above a threshold value. The shape of the electric field that spawns from the carbon nanotube in vacuum is also found to be near Gaussian [21].

1.4 The Optics of Nematic Liquid Crystals

The nematic mesophase is the one of the most common calimatic (rod-like) LC mesophases [22]. A large birefringence and a low control voltage distinguish the nematic phase from other electro optical materials. The molecules in the nematic phase only have long range order and no longitudinal order (i.e. do not form layers). This is the least ordered mesophase before the isotropic. The calimatic molecular shape gives order in the nematic phase, which means that on the average the molecules spend slightly less time spinning about their long axis than they do about their light short axis.

Fig. 1.9 Refractive indicatrix of a nematic liquid crystal molecule
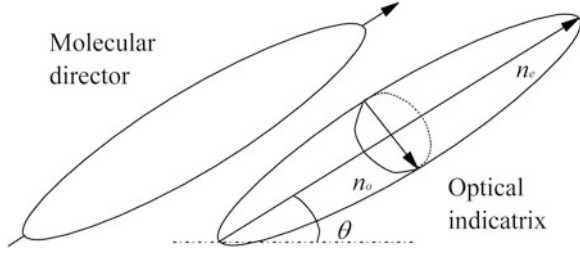
The optical indicatrix or index ellipsoid of a liquid crystal is a 3D structure to represent the variation of the velocity of light passing through it with respect to the molecular director. When light enters a birefringent material like a liquid crystal, its electric field is split into two orthogonal components termed ordinary and extra ordinary rays corresponding to the ordinary refractive index (n_o) and extra ordinary refractive index (n_e) as shown in Fig. 1.9. In the case of uniaxial samples, one of the components lies on the equatorial plane and always has the same value, called ordinary component. The other component varies with the angle of incidence and is known as the extra ordinary component. All these parameters are bulk parameters, which are estimated by taking the statistical average across billions of individual molecules.

If the optical indicatrix is oriented at an angle θ to the plane of the cell such as the plane of the glass walls and ITO electrodes, then the refractive index seen by light passing perpendicular to the cell wall is given by

$$n(\theta) = \frac{n_e n_o}{\left[n_e^2 \sin^2 \theta + n_o^2 \cos^2 \theta\right]^{\frac{1}{2}}}. \tag{1.14}$$

From the above equation, the optical retardance Γ can be calculated for a given sample of thickness d and at a wavelength λ when the material is oriented at an angle θ to the light polarization direction.

$$\Gamma = 2\pi d(n(\theta) - n_o)/\lambda. \tag{1.15}$$

The main properties that are used in our holographic and nanophotonic device developments are birefringence, dielectric anisotropy and fluid viscosity.

- Microscopic Anisotropy + ordering → Macroscopic Anisotropy
- Fluidity → Permits reorganization.

The speed of light in a medium is a direct function of the refractive index of that medium. Birefringent materials have refractive indices that are direction dependent. If the refractive indices for parallel and perpendicular polarised light are different within a material, then the light will travel at different velocities depending on its polarisation (the orientation of the electric field) through the birefringent medium. Interaction between the light waves polarised parallel and perpendicular to the molecular axis, depend on the wavelength and give rise to different colours when

viewed through an optical microscope with white light. Dielectric anisotropy of liquid crystals may be defined as the difference between the dielectric permittivities parallel and perpendicular to the director. Interaction of a liquid crystal with the external electric field is very much dependent on their dielectric properties.

1.5 Carbon Nanotube Plasmonic Devices

The optical properties of individual multi-wall CNTs (MWCNTs) are defined by their dielectric function, which is anisotropic in nature and matches very closely with that of bulk graphite [23]. However, the highly dense periodic arrays of MWCNTs display an artificial dielectric function, with a lower effective plasma frequency in a few hundreds of terahertz. Pendry [24] demonstrated that the electromagnetic response of a metallic array composed of thin metallic wires, excited by an electric field parallel to the wires is similar to that of a low-density plasma of very heavy charged particles, with a plasma frequency ω_p:

$$\omega_p^2 = \frac{2\pi c_0^2}{a^2 \ln(a/r)} \tag{1.16}$$

where c_0 is the velocity of light in vacuum, a is the lattice constant of the 2D wire array, r is the radius of the wires. This concept can be used for lowering the plasma frequency in the nanotube based applications and achieving negative dielectric constant for producing metamaterials. The lowering of the plasma frequency is due to the increase in the effective electronic mass on the nanotubes due to the induced current and corresponding magnetic field around them. According to (1.16), the effective plasma frequency strongly depends on the nanotube radius and lattice constant. Their values can discretely be chosen to engineer the MWCNT arrays of a desired frequency. The resultant frequency dependent permittivity can be calculated using the Drude model for metals [25, 26] described as

$$\varepsilon(\omega) = 1 - \frac{\omega_p^2}{\omega^2} \tag{1.17}$$

The effective permittivity $\varepsilon(\omega)$ is negative for frequencies less than ω_p, therefore no wave propagation will take place inside the material. Electromagnetic waves propagation only occurs above ω_p, due to which the structure acts as a nanophotonic high-pass filter. The structure was realized with square lattice array of MWCNTs having radius of 50 nm and lattice constant of 400 nm. The growth of high a/r aspect ratio arrays of MWCNTs was a significantly difficult task overcome through e-beam lithography and optimized growth recipe. To the best of our knowledge such highly dense periodic arrays of nanotubes have not been accomplished by any other research groups. Such small lattice constants are only reported in non-periodic patterned CNT growth or forests form growth of CNT arrays.
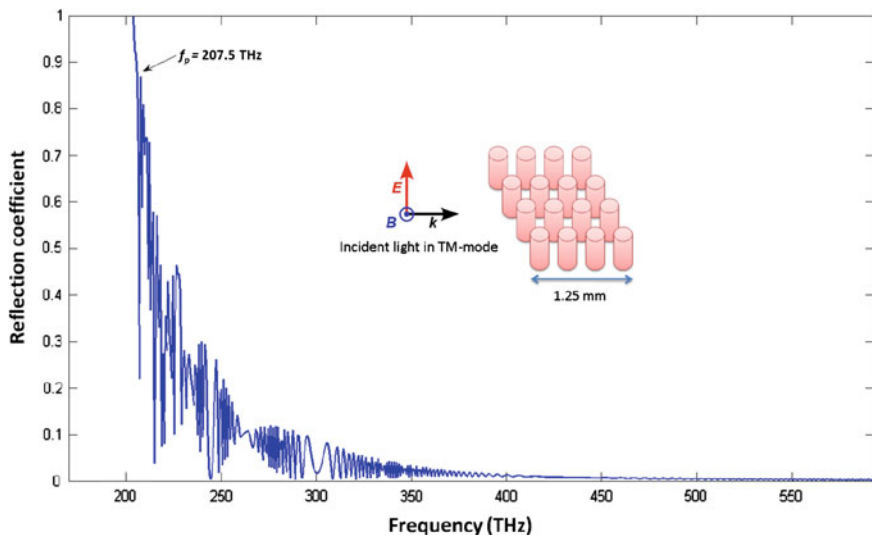
Fig. 1.10 The calculated reflection coefficient for a CNT based plasmonic high pass filter. At plasma frequency of 207.5 THz a sharp drop in reflectivity is calculated. The incident light is polarized parallel to the wire structure

The frequency dependent reflection coefficient was calculated as shown in Fig. 1.10. A sharp drop in the reflection is calculated at the plasma frequency, displaying a high transmission of the electromagnetic waves with larger frequencies [11]. The small peaks in the plot can be attributed to the multiple reflections at the interfaces. The result significantly matches the band gaps simulations of a 2D square lattice array of MWCNTs. For an array of the same lattice aspect ratio and incident light polarized parallel to the nanotubes (transverse magnetic (TM) mode), a band gap is observed close to the plasma frequency. However, in transverse electric mode (TE) (light polarized perpendicular to the nanotubes) no significant reflection band was observed in this regime, suggesting the plasmonic response of the structure in strongly dependent on polarization of the incident light.

To achieve this plasmonic high pass filter in the optical domain, metallic cylinders of nano-scale dimensions and interspacing are required. MWCNTs are promising materials to establish such metamaterials structures and the advancement in nano-technology facilitates the fabrication of high a/r aspect ratio nanotube arrays. Square lattice arrays of vertically aligned MWCNTs were grown on silicon substrates. An array of individual nanotubes is shown in the electron microscopy image of Fig. 1.11a and with a higher magnification view in Fig. 1.11b.

Due to the small lattice constant the nanotubes were tangled at various regions of the substrate. Additionally, some array defects were produced due to inhomogeneous depth of the nickel catalyst layer, affecting the decomposition of the carbon source, and hence, producing shorter MWCNTs. However, a steady periodicity required for a 2D square lattice was common throughout. Achieving longer
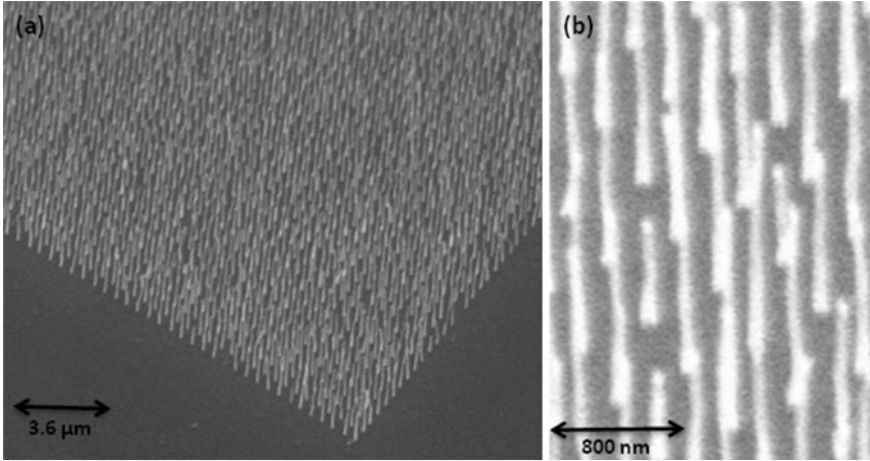
Fig. 1.11 a Electron microscopy image of a 2D square lattice array of MWCNTs having radius of 50 nm and lattice constant of 400 nm, grown on silicon substrate using PECVD. **b** The same in higher resolution

MWNCTs also remains a difficult task. Beyond the height of 4 μm the nanotubes become fairly thin leading to their tips collapsing with the neighboring tubes. Growth of longer tubes will require further optimization of the plasma generation technique and stronger electric fields for the vertical alignment of the tubes. According to the theory [24] the height of the wire structures must be longer than the operating wavelengths. Therefore, a MWCNT height of 2 μm was sufficient for this study as it established an aspect ratio (height to radius) of 40 and is longer than the plasma wavelength $\lambda_p = 1.45$ μm ($\lambda_p = c_0/f_p$) of the material.

The measured reflection spectrum at near normal incidence for light polarized parallel (TM) and perpendicular (TE) to the nanotubes is shown in Fig. 1.12. It shows a rapid drop in reflection after a frequency of 207.3 THz and significantly matches the calculated plasma frequency of the sample. Some small peaks were observed which can be explained by the defects in the periodic array of MWCNTs. The spectrum with light polarized perpendicular to the nanotubes did not show any significant cut-off effect, showing that most of the light was transmitted. However, a rapid drop in reflection at f_p for parallel polarized light shows that the periodic array of MWCNTs acts as high pass filter for near optical frequencies. The plasma frequency for the metamaterial can be further reduced into the optical regime by increasing the material density of the sample, i.e. by increasing the radius of the tubes and decreasing the lattice constant as presented in (1.15). Growth of well aligned MWCNTs at interspacing of less than 500 nm was a considerable achievement. Smaller lattice constant can be achieved by optimizing the catalyst layer and growth time in the PECVD process [27].

The results in Fig. 1.12 show how plasmonic effects in MWCNT arrays can be harnessed to control light in an effective manner. Ideally we could now add a
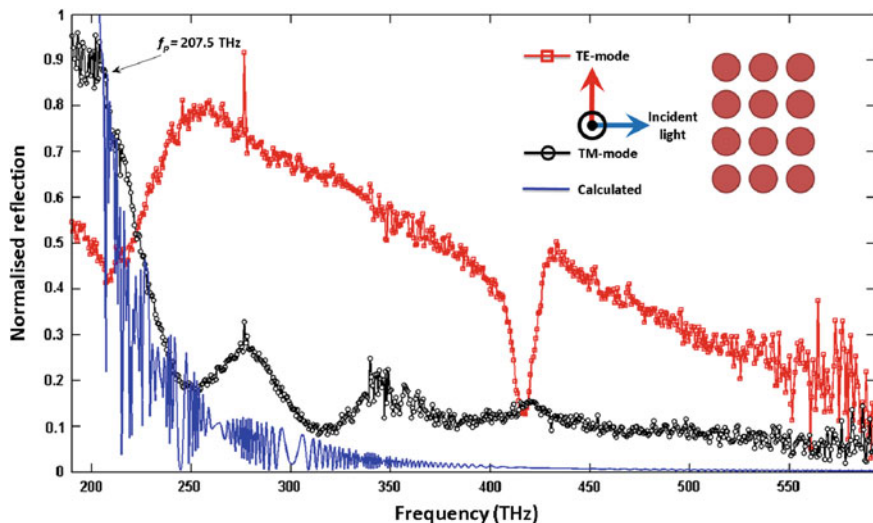
Fig. 1.12 The reflection measurement from the sample for light polarized parallel (*TM*) and perpendicular (*TE*) to the multi-walled carbon nanotubes. A sharp drop in the reflected TE-mode is observed at plasma frequency (207.5 THz) which significantly matches the theoretical result. No such cut-off effect is observed for the TE-mode

liquid crystal material to the arrays of MWCNTs, allowing us to vary the refractive index about the CNTs with an applied electric field and therefore allow us to vary the plasmonic resonant cut off. Unfortunately adding a higher refractive index material to (1.15) pushes the plasmonic resonance further into the longer wavelengths (near infrared) which does not simplify the processing of characterising these devices. In order to reduce the plasmonic resonant frequency into the visible regime, MWCNT spacings of around 100 nm would be required which has not yet been possible using PECVD techniques. As will be seen on the following sections, the light does not have to illuminate the MWCNTs parallel to their length in order to excite plasmonic effects. Light can be incident along their length and still see plasmonic effects due to the excitement of the electrons across the lateral diameter of the MWCNTs [28]. The physics of this process is not yet fully understood, however there have been successful observations of this effect which can be used to create MWCNT based diffractive holograms.

1.6 Quasi Crystalline Diffraction from Nanotube Arrays

A very effective demonstration of enhanced plasmonic effects from laterally illuminated MWCNTs has been demonstrated by the diffraction patterns observed from a 2D Penrose tiled quasicrystal structure [29]. This structure has been seen

previously by etching air cylinders into a quartz substrate [30], where laser light at 633 nm was transmitted through the dielectric quasi-crystal formed by the air cylinders in the quartz and relatively weak diffraction spots were observed. The air cavities were 3 μm in diameter, 700 nm in depth and placed 10 μm apart on a tile side (the pattern area was 0.013 mm^2). An alternative approach is to use a finer 'inverse' structure of quasi-periodic pentagonal arrays of MWCNTs on a Si substrate. The MWCNT diameter, related to patterned catalyst diameter, was 80–120 nm, and length 700 nm. The spacing between MWCNTs on a tile side was 1400 nm and the pattern area 2.5 mm^2. In contrast to the previous work, the MWCNTs act as an array of metallic nanometre scale rods forming a hologram for reflected light. This allows the reversibility of the optical waves from the light source through reflection to be exploited to get a "beaming" effect due to the plasmonic resonance and is often compared to that emanating from a phased array antenna. Since the MWCNTs are placed in a 2D quasi-crystalline array (i.e. having periodic breaking of symmetries), a rich diffraction pattern, or many spots are seen. The MWCNT arrays were excited with 532 nm laser light and the results compared with theoretical predictions of diffraction for crystals with tenfold symmetry. The flexibility and accuracy of the growth system used allows the production of array patterns over large areas on wafers up to 8″ diameter, so that the exciting beam of laser light falls entirely on the array without the need for complicated alignment procedures.

The calculation of the diffraction pattern for a periodic system revolves around the construction of the reciprocal lattice and subsequent placement of the first Brillouin zone; however, in this case the aperiodicity of the pentagonal array requires a different approach due to the lack of translational symmetry. The reciprocal lattice of such an array is densely filled with reciprocal lattice vectors, with the consequence that the wave vector of a transmitted/reflected light beam encounters many diffraction paths. The resultant replay fields can be accurately calculated by taking the FT of the holograms. To perform the 2D fast Fourier transform (FFT) of the quasi-crystalline nanotube array, a normal scanning electron micrograph was taken, as shown in Fig. 1.13.

The Si wafer bearing the pentagonal array was mounted onto a post with a flat screen set above it. The plane of the screen is parallel to the plane of the sample and the screen has a small aperture in its centre. A 532 nm (green) laser was mounted above the screen, arranged so that the beam was normally incident at the sample. The reflected diffraction pattern produced when the sample was illuminated was captured by a camera and corrected for distortion due to the off-axis camera position. The observed diffraction pattern is in very good agreement with the calculated results. A comparison of the two is presented in Fig. 1.14a, b. The pattern order also shows good agreement when compared with the Penrose reciprocal lattice calculated using the five lattice vectors, Fig. 1.14c. The diffraction pattern in Fig. 1.14b shows bright outer spots which correspond to the superposition of two pentagrams rotated by angle π/5 with respect to each other. The Penrose tiling as seen in the SEM image of Fig. 1.13a is generated from "fat" and "skinny" rhombi (P3 group), whose base angle is π/5.
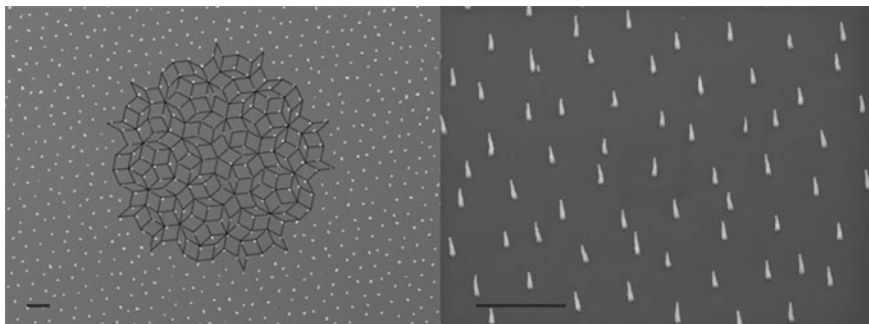
Fig. 1.13 SEM images of a quasi-periodic array of carbon nanotubes. *Left panel* Normal view, with Penrose tile scheme overlaid. *Right panel* Array tilted by 45°. Scale bars 2 μm. CNT heights are ∼700 nm
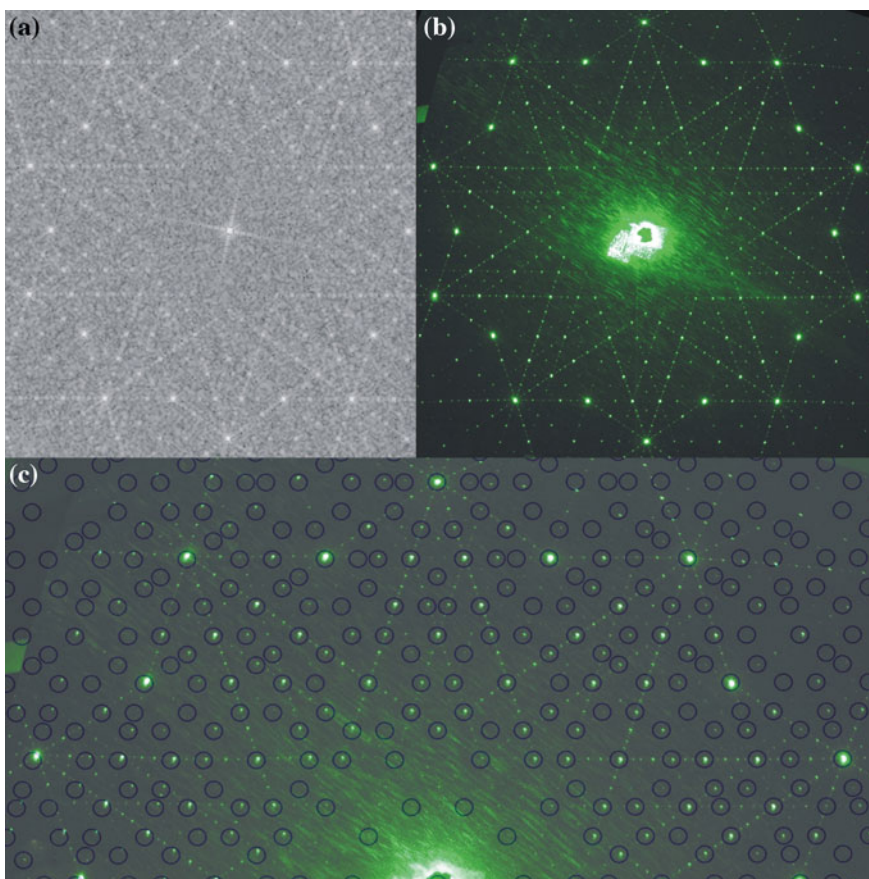

Fig. 1.14 Comparison of **a** FFT of SEM image of pentagonal array nanotube tips, **b** diffraction of normally-incident *green* laser light (the *dark central* spot is the aperture in the screen through which the laser enters) and **c** shows an overlay of the reciprocal lattice points as calculated onto half of the laser diffraction pattern
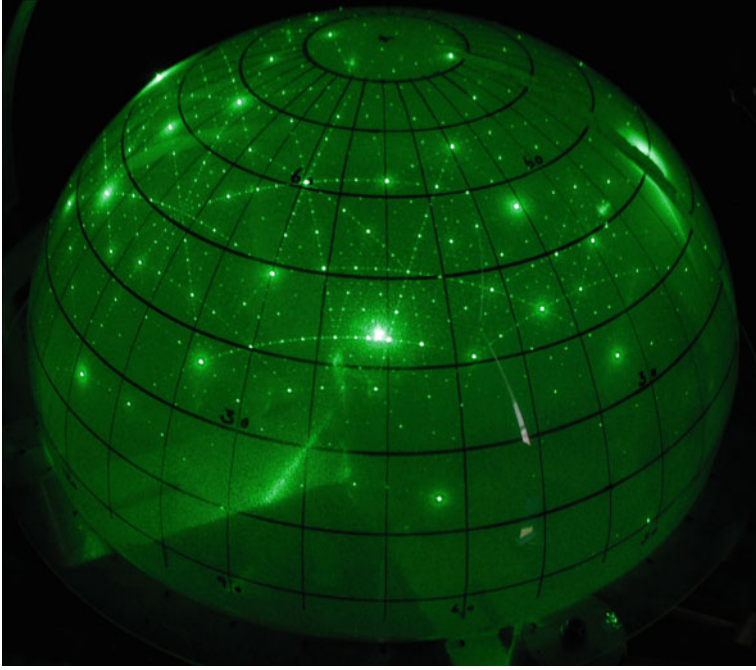
Fig. 1.15 Penrose diffraction of 532 nm laser, incident at an angle of 5Å from the normal, captured with a semi-transparent dome

The remarkable "richness" and intricacy of the optical replay field emanating from the quasi-crystalline MWCNT array is best seen in the spherical diffraction pattern shown in Fig. 1.15. The results clearly show that the quasiperiodic array of nanotube antennas act as holograms (apertures) for the reflected light, producing remarkable and striking diffraction patterns (replay fields).

These patterns are complimentary to the materials that have shown patterned MWCNT arrays which form a regular 2D crystal can also be used to obtain metamaterial properties associated with nanoscale metal wires [11]. In this mode the reduced plasma frequency in the MWCNT due to induced current flow in the axial direction and the resulting circumferential magnetic field is exploited to obtain a negative permittivity in the optical frequencies In the quasi-periodic array used here r is nominally 100 nm and the spacing a between them is 1400 nm. Given that the permittivity function as a function of plasma frequency given by (1.17). The negative permittivity regime, when no light can be transmitted into the array, will only result at wavelengths larger than $\lambda_p = 5700$ nm. The optical wavelengths at which the diffraction is measured are well below this. Hence light transmission into the MWCNT array is not prohibited. On the other hand the orientation of the axes of the MWCNTs is normal to the plane of incidence of the

EM. This makes both the electric and magnetic field components normal to the MWCNT axis.

Micro-scaled patterns of light resulting from the quasi-periodic MWCNT arrays as shown here are difficult to replicate/forge. A ready application for them would therefore be for security purposes such as to validate the originality of brands, passports, cheques, important documents etc. They can also be used, in either periodic or quasi-periodic form, for directing a single beam of coherent light to many spatial locations simultaneously. There could of course be many other applications hitherto not foreseen, such as optical coding, where the rich and layered diffraction patterns resulting from these 2 dimensional quasi-crystals can utilised.

1.7 CNT Based CGH Holograms

As seen in the case of the quasi-crystalline structures, the far field diffraction patterns (and the field of view) are dictated by the pattern of the carbon nanotube arrays. The next objective is to control the angular diffraction from CNT array by fabricating these arrays in the form of CGH patterns. The array of nanotubes acts like a hologram (grid of apertures) towards the incident light, producing a diffraction pattern (in this case the word CAMBRIDGE) in the far field [31]. This replicates the mechanism of an optical projector or spatial light modulator while using the world's smallest pixel defined by a nanoscaled carbon nanotube. Fourier optics was utilised to calculate the MWCNT array (hologram) that would produce a CAMBRIDGE image in the replay field. The methodology used was to optimize a binary amplitude intensity mask using the Gerchberg–Saxton algorithm [16]. The CNT hologram was modeled as a square array of 300×300 pixels spaced by a lattice constant of 400 nm and a tube radius of 50 nm. Through an iterative process the optimized binary intensity hologram (carbon nanotube array) was calculated as shown in Fig. 1.16 with its corresponding replay field. The several orders of symmetrical conjugate images were as predicted for the hologram. The calculations were performed based on the principle of diffraction optics assuming the carbon nanotubes acted as diffracting elements. The calculations did not directly take into account near field optical effects like surface plasmons, usually attributed to nanophotonic structures like carbon nanotubes.

Based on the calculated CGH pattern in Fig. 1.16 the fabrication of carbon nanotube array was fabricated on a 10×10 mm silicon (Si) substrate. A growth time of 15 min at a pressure of ~ 3 mBar yielded a MWCNT array with a tube length of approximately 1500 nm. Scanning electron microscrograph (SEM) of the fabricated nanotube array is shown in Fig. 1.17. A highly ordered array of vertically aligned MWCNTs was obtained with inter-nanotube spacings of ~ 400 nm. Figure 1.17c shows a cropped SEM image of the nanotubes CGH hologram taken from vertically above the substrate. It can be observed that the square lattice consist of less than 4 % of the nanotube area. The FT of this image is shown in Fig. 1.17d. The highly intense zero order due to the un-diffracted light has been
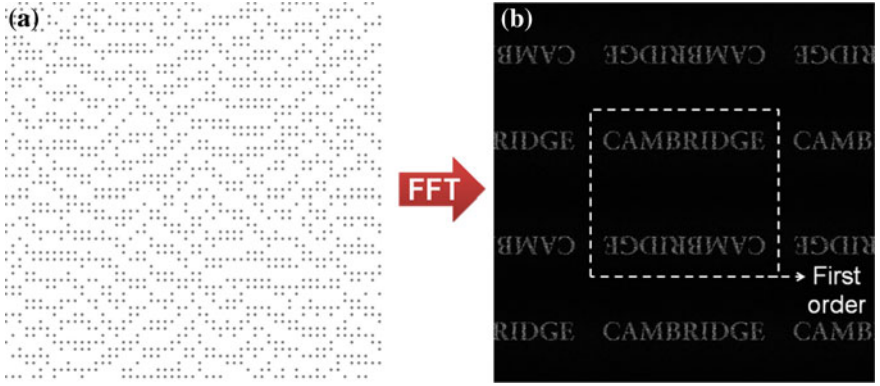
Fig. 1.16 The CGH designed. **a** 2D hologram based on 300×300 *square* array of multi-walled carbon nanotubes (lattice constant 400 nm). **b** FT of the CGH
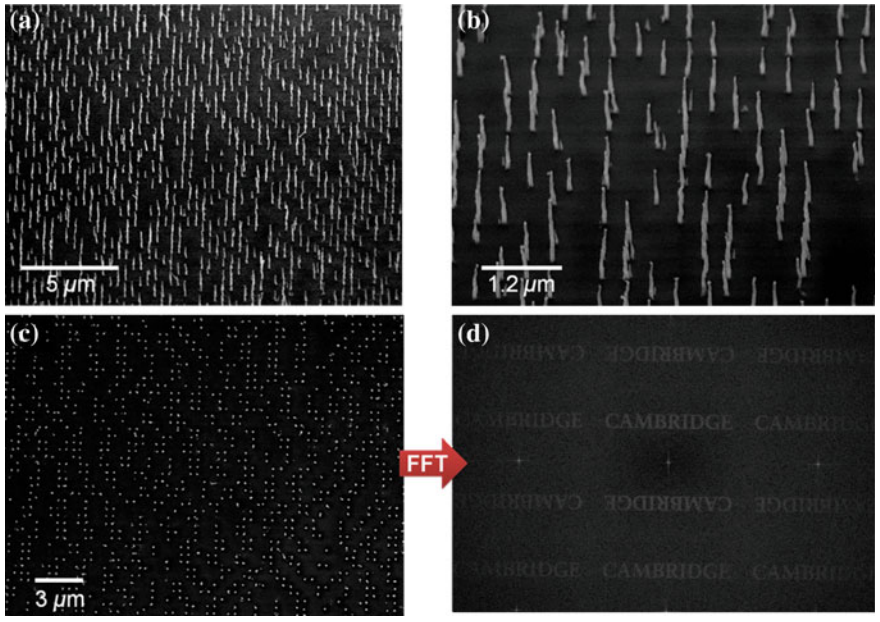

Fig. 1.17 Fabricated images of the carbon nanotube array. **a** SEM image of the fabricated MWCNT array (30° from vertical). **b** Higher magnification. **c** SEM image of the nanotube array taken at a normal angle. **d** 2D FT of the SEM image

removed from the image to make the image clearer, and the efficiency of the hologram was estimated at 4 %. The results showed that the nanotube array was accurately fabricated and could perform as a binary amplitude intensity hologram.

An optical characterization of the nanotubes CGH was undertaken next. The CGH was mounted onto a post with a semi-transparent hemispherical screen set above it. The hemispherical screen had a radius of 20 cm which allowed sufficient distance to capture diffraction patterns in the far field. The base of the screen was placed parallel to the plane of the sample and the screen had a small aperture in its centre to allow the passage of an incident laser as shown in Fig. 1.18a. A 532 nm laser was shone through the aperture, arranged so that the beam was normally incident to the sample. The reflected diffraction pattern produced when the CNT hologram was illuminated was captured using a digital camera.

Figure 1.18b shows the observed diffraction pattern which was in excellent agreement with the calculated results. The first order diffraction pattern (replay field) consisted of two symmetrically conjugate CAMBRIDGE images placed on opposing sides of the screen. The higher orders diffraction patterns were not observed as they were projected large angles ($>90°$ to the normal) due to the nanoscale periodicity of the MWCNT array. A high intensity zero order was observed consisting of the un-diffracted light which did not interact with the CNTs and was mostly reflected from the Si substrate. According to calculations around 94 % of the incident light should be present in the zero order as CNTs occupy only about 4 % of the area in the binary hologram. Under these circumstances the zero order should dominate the replay field and be bright enough to saturate the camera resulting in the first order not being visible. However, as observed in Fig. 1.18, the CAMBRIDGE pattern was clearly visible even in the presence of the zero order suggesting the CNT based hologram presents higher diffraction efficiency than expected. Later testing indicated that the diffraction efficiency was more like 25 %, which indicates that the hologram is performing more than just amplitude modulation This is related to the highly metallic character and large effective scattering cross-section of the MWCNTs [28] which allows them to act as exceptional optical scattering elements.

Also the nanoscale dimensions of the CNT array ($a = 400$ nm) causes the diffraction of light at large angles increasing the field of view. According to the principle of Bragg diffraction the diffraction angle is dependent on wavelength and lattice constant. The diffraction patterns from the MWCNT hologram were studied under blue (454 nm), green (532 nm) and red (635 nm) lasers. With the increase in laser wavelength the image was diffracted at larger angles producing larger images. The effect was consistent with Bragg's law. The red laser image was diffracted to the largest angle of around 35° from the vertical. Furthermore, in contrast to the conventional 2D holograms, CNT arrays have a 3D structure that causes the optical diffraction in an anisotropic manner. The diffraction from nanotube arrays was expected to be dependent on the angle of incidence and the polarization of light. The diffraction efficiency measurements were performed by measuring the intensity of light in the zero and the first order. The first order image was measured by placing a high numerical aperture lens near the sample to focus all the diffracted light into the photodiode. Measurements were performed with red laser light polarized parallel and perpendicular to the axis of the carbon nanotubes.

Fig. 1.18 Experimental setup and measured diffraction pattern results. **a** The experimental setup employed to capture the diffraction pattern. **b** The pattern was obtained on a semi-transparent hemispherical screen
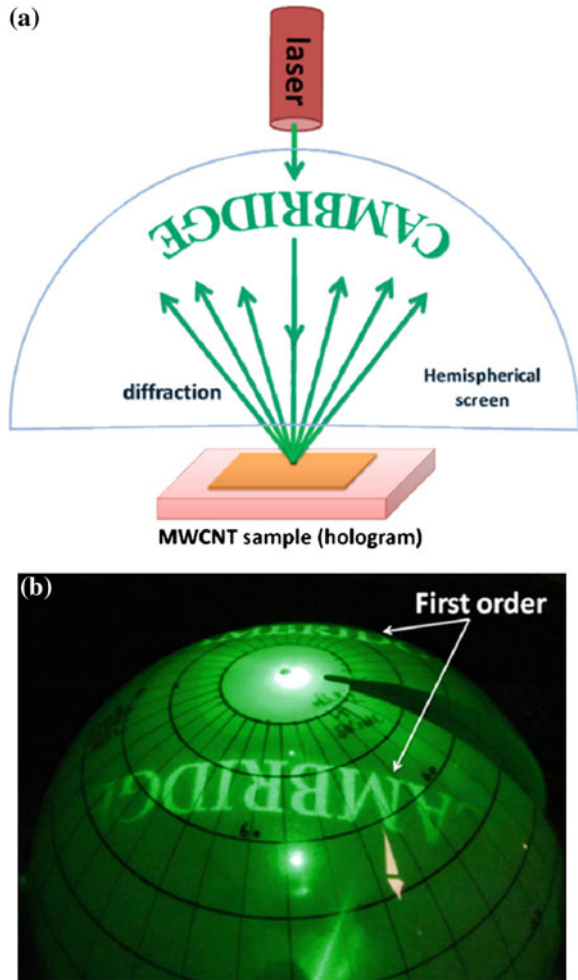
The role of the MWCNT plasmonic effect is still not completely understood in this work, however there is a clear potential for these devices to increase the capabilities of future optical systems. The ability to control light using these structures can be further enhanced using liquid crystal materials and several devices have been made which combine the ability to control the light through plasmonic resonance with the variable refractive index of a LC material. Figure 1.19 shows a 400 nm spacing MWCNT similar to the one shown in Fig. 1.12. BLO006, a nematic LC mixture from Merck was added above the array in a 10 μm thick layer using an ITO coated glass top substrate with rubbed polyimide alignment. As the Si is conducting it is possible to place an electric field across the cell and switch the LC material.
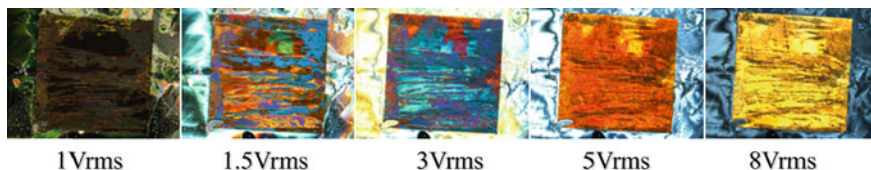
Fig. 1.19 A 400 nm pitch MCWNT array with 10um of nematic LC seen between crossed polarisors at different applied electric fields

The images shown in Fig. 1.19 show the colour changes induced by applying an electric field. These colours are much more vivid than the ones seen in normal nematic LC devices and are indicative of a shift in the Bragg grating wavelength of the MWCNT array. Further investigation of this effect has been hampered by the geometry of the devices and the difficulty in getting through cover glass (0.7 mm thick) in order to interrogate the LC/MWCNT combination. This limitation is both tantalizing but also shows that this type of structure is inherently limited by the growth direction of the MWCNTs. In order to see what sort of effects might be possible using these sorts of materials, a better resonant structure is needed which allows much easier access to the resonant features.

1.8 Nanophotonic Antennas

An alternative geometry to the vertically grown MWCNT arrays is to create nanophotonic structures that are parallel to the substrate (i.e. laying on the surface). Such structures in this geometry are often referred to as antennas as they have similar field properties to the larger scale versions used in communications technology. This form of plasmonic nano-antennas has been of interest due to their unique optical properties [32]. For instance, a perfect conducting rod with a negligible skin depth will have a half-wave dipolar resonance when the length of the long axis is equal to any multiple of half the wavelength. In contrast, when the polarisation is rotated towards the short axis the resonant conditions change. A critical criterion to consider is that antennas do not scale linearly across the whole spectra. The reason for this is that at short wavelengths the skin depth has a comparable size with the antenna. Hence, radiation penetrates into the metal and gives rise to oscillations of the free-electron gas within. Consequently, the effective resonant wavelength inside the metal can be reduced to a fraction of the size [33, 34]. Although this scalability disproportion might seem a problem from the fabrication point of view, a nano-antenna with sub-wavelength sizes allows one to widen the traditional concept of diffractive optics.

It has been proposed that sub-wavelength dielectric structures alter the effective medium without affecting the diffraction pattern in an optical system [35]. An expansion of the effective medium approach was also suggested for metals [36].

The effective medium theory can simplify the design of a hologram, but the effect of an individual nano-structure is not considered. A single carbon nanotube as a diffractive unit has been demonstrated in the previous section. In contrast with the effective medium theory, the scattering of a sub-wavelength structure was used as a diffractive unit. Interestingly, when these nano-structures have large scattering cross section, the diffraction effect is highly enhanced [28, 31]. It is not uncommon that a metallic nano-structure scatters above five times more light than that calculated purely from its geometrical cross-section. Another completely different approach is selectively and simultaneously illuminating different nano-structures with a predefined field to superpose their radiation as eigenmodes, so patterns of only a few pixels can be reconstructed.

In order to produce a diffractive effect, it is necessary that electrons in all of the nano-antennas resonate in phase producing a coherent source. When a laser beam is applied normal to the hologram plane, it is possible to induce emissions in phase. However, only those nano-antennas oriented in the direction of the electric field will emit. This means that by changing the incident light polarisation the nano-antennas can be "switched on" or "switched off". To take advantage of this we have superposed two transversal polarisations at a sub-wavelength distance. This is based on the assumption that two off-axes dipolar antennas with transversal polarisations have minimal coupling. In the case of particles, it has been suggested that dipolar coupling is negligible when the distance between them is larger than ~ 3 times the radii [37]. To avoid the interaction between transversal polarisations we have chosen to place two nano-antennas in an "L" shape separated by a fixed distance. This task would be impossible with typical antennas if the pitch of the sampled hologram was the same as the antenna length. However, in the case of optical nano-antennas, this is easily achievable with a wide separation between them. In contrast, if coupling is required, a "T" shape can produce an anisotropic interaction between the nano-antennas in one of the polarisations.

The steps to produce a hologram start with two arbitrary and independent designs either in two-dimensions or three-dimensions. Each of those designs represents the reconstructions for the relevant transversal polarisation. The diffraction pattern is then obtained by using a retrieving algorithm for CGHs [16]. Once the diffractive pattern is obtained, the sampling process should be performed. In this step, the two independent holograms have to be sampled giving the two transversal nano-antennas. A square grid is optimum due to its geometrical match with the two transversal polarisations. The last step in the hologram design consists of merging the two holograms. To maximise the inter-antenna distance, each hologram has to be shifted by half the sampling pitch in both directions. The displacement between antennas shifts the phase of the reconstruction without altering the intensity pattern. Figure 1.20 shows the design process and the final "L" shape formed by both transversal nano-antennas.

In order to prove the concept, the nano-antenna characterization had to be performed on a suitable device. The metal chosen was silver because of its favourable plasmonic properties in the visible spectrum [39]. The optimum parameters for the nano-antennas were calculated according to literature [34],
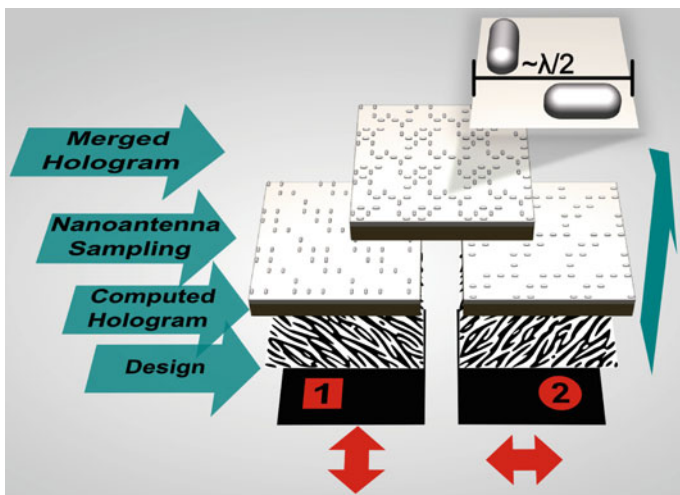
Fig. 1.20 The hologram design consist of four steps: the digital creation of two independent images for each polarisation, the retrieval of independent diffraction patterns, the nano-antenna sampling of the fringes and finally the blending of both sampled designs

simulations, and experiments. The nano-structure chosen was a nano-rod with dimensions of about 60 nm in diameter and 170 nm in length. This nano-antenna showed a strong emission for the red wavelength (650 nm) with a polarisation in the direction of its long axis and no interaction with the transversal polarisation. We tested experimentally our approach by evaluating each hologram in the far field. The target of the two transversal polarisations consisted of two independent images, one containing a square with an inscribed number "1" and the other containing a circle with an inscribed number "2". The independent CGHs that reconstruct these images were retrieved using the Gerchberg-Saxon algorithm. A computer program was developed to generate two arrays of 250×250 nano-antennas with a pitch of 390 nm. Finally the two sampled CGHs were merged into a single overall hologram pattern.

The nano-antennas where fabricated on top of a 200 nm silicon dioxide layer on a standard silicon wafer. The substrate was spin coated with high resolution positive PMMA 950 K resist and electron beam lithography was used to define the nano-antenna structures. After exposure, the samples where developed in a MIBK:IPA solution with a 1:3 composition. Finally, silver was thermally evaporated and lifted-off to remove of the unwanted residual metal areas. The total number of nano-antennas created was 6.25×10^6 distributed over an area of 2.13 mm^2. Although the final array of nano-antennas was laid on top of a dielectric layer of silicon dioxide, the silicon substrate obstructed the transmitted light. In Fig. 1.21, SEM pictures at different magnifications show the obtained results through this process. The two transversal nano-antennas in an "L" shape form a
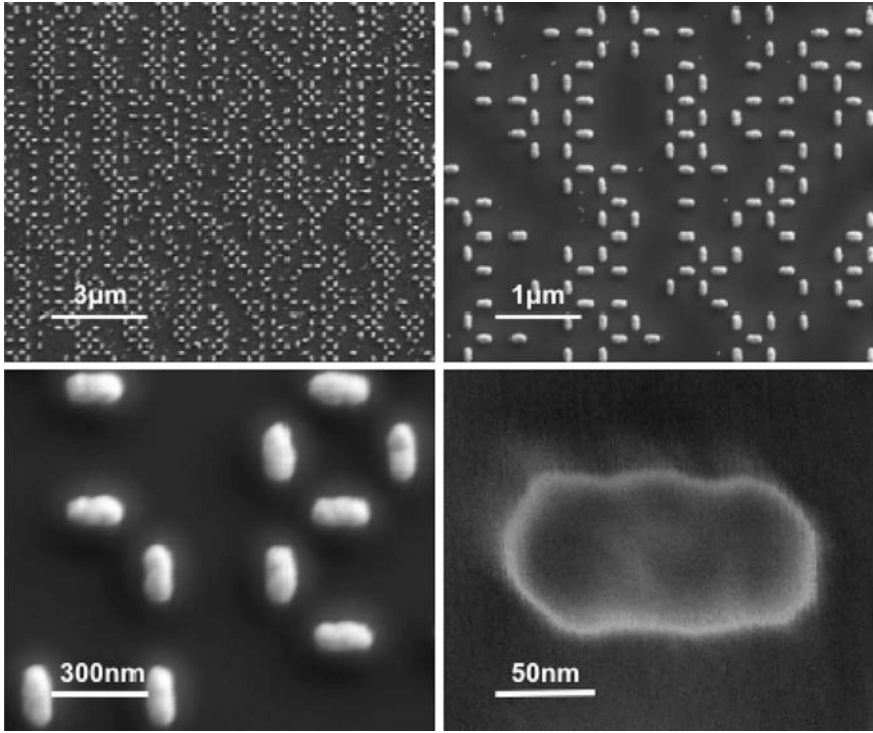
Fig. 1.21 *Four* different magnifications of a section of the fabricated CGH

large array with a profile similar to a weave. The dimensions of the nano-rods are uniform but some roughness can be observed on the surface of the nano-antennas.

The upper part of Fig. 1.22 shows the simulation of the projected waves for polarisations at $0°$, $45°$ and $90°$. The simulation shows the intensity of the field at the boundaries of the two transversal nano-antennas from a single diffractive unit of 390 nm × 390 nm. Additionally, it shows the field intensity in two different planes, one at 20 nm and the other at 120 nm from the top of the nano-antenna. The intensity at the boundaries (and the first plane) shows the dipolar behaviour while the second plane shows the radiated far-field. It can be observed, that the interaction occurs mainly when the electric field of the light is oriented in the direction of the long axis, so the radiated pattern in transversal polarisation is negligible. It is interesting to note that the polarisation oriented at $45°$ induces a resonance in both antennas equally. Simulations were performed with the boundary element method as shown in [38]. The real reconstruction was observed experimentally by using a low intensity polarised laser diode (650 nm) in a direction normal to the hologram plane. The image is switched just by rotating the laser along the normal axis. The images in the lower part of Fig. 1.22 show the projected image on a semi-transparent sphere (half a ping pong ball) for the
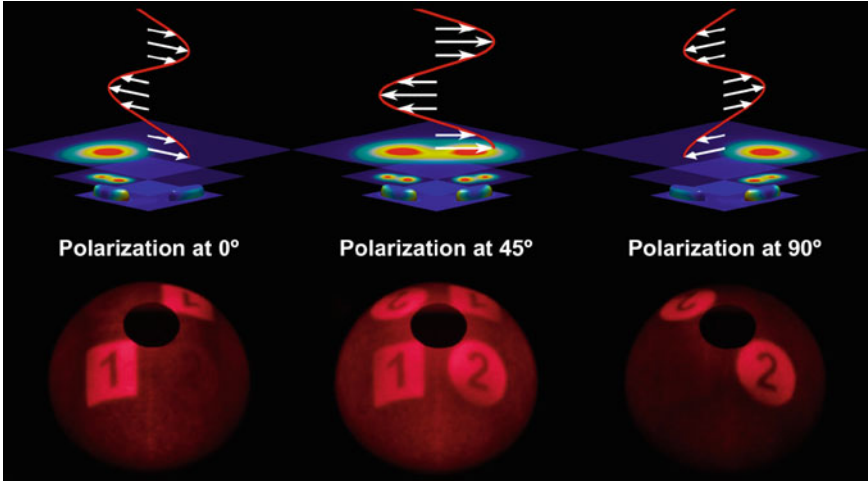
Fig. 1.22 Simulations (*upper half*) and experimental results (*lower half*) for two independent holograms at $0°$, $45°$ and $90°$

excitation of the two independent nano-antenna CGHs. In addition, the $45°$ image shows the excitation of both polarisations producing the two images simultaneously. The reconstruction background noise covers the antenna radiation pattern as an envelope across the whole sphere. This pattern represents an important characteristic of a diffractive antenna array, the two opposite lobes are imaged in the direction of the axis for each excited antenna. Also, the intensity does not decrease at large diffractive angles, in contrast with diffractive optical elements based on embossing or relief, nano-antennas can be highly omnidirectional [39] and holograms can achieve a wide field of view with a uniform angular intensity distribution. This CHG produced a field of view of $112.8°$.

The relation between diffracted intensities in the far field produced by both polarisations can be found by projecting the component of the electric field vector in the nano-antenna resonant axis. The solution is given by $I_i cos^2(\theta)$, where I_i is the intensity of the incident beam and θ is the angle between the resonant axis and the electric field vector. This solution is similar to a pair of polarisers, but in this case the solution represents the diffraction produced by radiated light. We have proved this by measuring simultaneously the intensities of both diffracted images (see Fig. 1.23a). The polarisation extinction ratio in our experiments is minimal. The polariser used had an intrinsic leakage of about 1 %, but according to simulations, the transversal resonance of the silver nano-antenna used is about 5 % with respect to the parallel resonance. However, the transversal resonance does not necessarily radiate in an omnidirectional way, and therefore its intensity might be even dimmer in the far-field (this transversal resonance can be decreased even further with optimization).
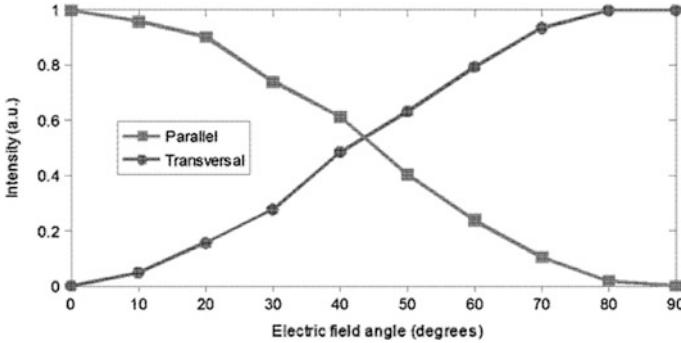
Fig. 1.23 Intensity relation of the two diffracted emissions for an electric field oriented at different angles

The total back-scattered efficiency measured at the far-field with a 650 nm beam was around 3 % with respect to the zero order. However, this is not a clear picture of the real diffraction efficiency because our samples couple most of the light inside the silicon dioxide layer which then gets trapped or absorbed by the silicon wafer. Catchpole showed that hemispherical shapes couple around 90 % of the light into the substrate [40]. Furthermore, silver nanoparticles in these dimensions have a negligible absorption comparing with their scattering. Through an alternative measurement of the zero order, it was found that about 17 % of the light incident on our samples was scattered (considering minimal absorption). This figure seems to be more reasonable if the total geometrical fill factor of the nano-antennas is about 3 % and the scattering cross-section enhances the diffraction by a factor of 5. Hence, we can predict that the efficiency can be highly enhanced by using forward scattering with a transmissive substrate and by matching the refractive index of the substrate.

From this work we see theoretical approach to control the emission of nano-structures by exploiting the plasmonic properties of anisotropic nano-structures. Hence, we have fabricated a switchable CGH capable of reconstructing high resolution images along a wide field of view. The next stage is then to create dynamic switching of the CGH by using a nematic LC material to control the incident polarisation state onto the antennas. Equation 1.15 states that if the LC material is oriented to give a half wave retardance ($\Gamma = \pi$), then the incident polarisation state can be rotated by 90°, flipping from horizontal to vertical (or vice versa). To test this, a nano-antenna substrate was assembled into a LC device using the same structure as that used with the MWCNT array. 10 µm of the nematic LC mixture BLO006 was placed between the array and a glass top substrate with both an ITO electrode and also a rubbed polyimide alignment later. In this device, the rubbing direction was set to as to create planar alignment of the LC at 45° to both directions of the nano-antennas (i.e. it split the "L" of the structure designed). The means that when the LC is set to be a half wave plate, then the polarisation of

Fig. 1.24 Experimental images from the LC/antenna device. *Left*, 0 V applied (*vertical*). *Centre*, 0.44 Vum^{-1} applied (45°). *Right*, 0.65 Vum^{-1} applied (*horizontal*)

the incident light will be flipped from one set of antennas to that of the orthogonal set.

Figure 1.24 shows the experimental testing of this device with an applied electric field between the Si and the glass substrate (i.e. across the nematic LC). The first image shows the replay filed from the CGH measures using a 650 nm laser, with its polarisation axis aligned to be parallel to the vertical array of nano-antennas. As a result, the word "CAMBRIDGE" can be seen produced by the diffraction from this array. As the applied electric field across the LC is increased, the polarisation of the incident light is rotated and both replay fields can bee seen in the centre image of Fig. 1.24. The image now shows both replay images (the word and also an image of Kings College Chapel) together, as both CGHs are being excited by the incident light. The final image on the right of Fig. 1.24 shows a further increase of the applied electric field to 0.65 Vum^{-1}, and the work CAMBRIDGE is extinguished. This image is very difficult to obtain with this setup, as there is a degree of polarisation wander from the laser, and the rotation of the laser must be made to keep the system stable. The array is also very sensitive to the applied electric field, as the response of the LC is quite steep and difficult to maintain with the voltage source used in this experiment. All three images in Fig. 1.24 were obtained for the same orientation of the laser and purely by variation of the applied electric field.

The results shown in Fig. 1.24 show preliminary switching of the polarisation state for an applied electric field across the nematic LC. Better results could be obtained using a more stable setup, but these results are still very important to the understanding on LN nano-photonic devices. The change in orientation of the nano-structures has allowed polarisation to be interrogated in a much more rigorous way than was possible with the LC/MWCNT devices. Hence it is possible to conclude that the plasmonic resonance of these structures is maintained within the LC and is not affected by the interface with the LC. It also shows that it is possible to engineer suitable device structures based on hybrid combinations of these technologies using solid physical and engineering principles, to give predictable device performance.

1.9 Conclusions and Discussion

In this chapter, we have presented a nanophotonic device based on a hybrid combination of multi-walled carbon nanotubes, silver nano-antennas and LCs. The carbon nanotube electrode arrays were grown on silicon substrate by plasma enhanced chemical vapour deposition after employing e-beam lithography and covered with nematic LC. The multi-walled carbon nanotubes act as individual electrode sites that spawn an electric-field profile, dictating the refractive index profile within the liquid crystal and hence creating a series of graded index profiles, which form various photonic elements. The device was analyzed under an optical microscope and it was found that photonic element was formed at each nanotube site and the photonic elements switched with respect to the applied voltage. This has lead to the conclusion that micro/nano regions in the device interact with light. The silver nano-antennas were fabricated using a standard lift off procedure and created structures that exhibited plasmonic resonances at visible wavelengths.

Both of these nano-photonic structures were combined with classical CGH design techniques to control light by diffraction. Both proved very successful and both also exhibited a higher degree of efficiency than was expected from a purely amplitude based hologram. This indicates that the plasmonic effects seen in the nano-structures are interacting with the light in a complex manner and creating a diffractive element with pixels that appear larger than have been fabricated. Both structures have also been combined with LC materials to create switchable nanophotonic devices. The MWCNT device showed a voltage dependent shift in the Bragg diffraction due to the periodic array of MWCNT. Further characterisation of the MECNT device is on-going to confirm the effect seen is plasmonic in origin; however the geometry of the device makes this very difficult to interrogate. The silver nano-antennas allow us to confirm the effects of the LC material directly through the observed switching in the polarisation state above the hologram. This demonstrates the ability to tune the plasmonic resonances to a particular polarisation state and then switch between the states using as LC material. Further devices are being fabricated which will further exploit this effect across both the polarisation states as well as the visible wavelength range.

The potential applications of this type of nanophotonic device range from 3D displays through to adaptive optics such as tweezers and wavefront sensors. Even more importantly these types of devices open up several new optical and electro-optical effects that can be used to control the light. If such effects were integrated into an existing display technology, then the possibilities are endless with both polarisation, wavelengths and spatial control selectable at the pixel level of the LC devices. Such innovations push the technology ever closer to replicating the sort of optical effects seen in classical photographic holograms.

References

1. B. Brown, A. Lohmann, Complex spatial filtering with binary masks. Appl. Opt. **5**, 967–969 (1966)
2. W. Lee, Sampled Fourier transform hologram generated by computer. Appl. Opt. **9**, 639–643 (1970)
3. A. Jendral, R. Brouer, O. Bryngdahl, Synthetic image holograms: computation and properties. Opt. Comm. **109**, 47–53 (1994)
4. M. Stanley et al., 100-Megapixel computer-generated holographic images from active tiling: a dynamic and scalable electro-optic modulator system. Proc. SPIE **5005**, 247–258 (2003)
5. R.H.-Y. Chen, T.D. Wilkinson, Computer generated hologram with geometric occlusion using GPU-accelerated depth buffer rasterisation for 3D display. Appl. Opt. **48**, 4246–4255 (2009)
6. D. Gabor, A new microscopic principle. Nature **161**, 777 (1948)
7. D. Gabor, Microscopy by reconstructed wave-fronts. Proc. Roy. Soc. (London) A **197**, 454 (1949)
8. E.N. Leith, J. Upatnieks, Wavefront reconstruction with diffused illumination and three-dimensional objects. J. Opt. Soc. Am. **54**, 1295–1301 (1964)
9. S. Tay, P.-A. Blanche, R. Voorakaranam, A.V. Tunc, W. Lin, S. Rokutanda, T. Gu, D. Flores, P. Wang, G. Li, P. St Hilaire, J. Thomas, R.A. Norwood, M. Yamamoto, N. Peyghambarian, An updatable holographic three-dimensional display. Nature **451**, 694–698 (2008)
10. T.D. Wilkinson, X. Wang, K.B.K. Teo, W.I. Milne, Sparse multiwall carbon nanotube electrode arrays for liquid-crystal photonic devices. Adv. Mater. **20**, 363–366 (2008)
11. H. Butt, Q. Dai, P. Farah, T. Butler, T.D. Wilkinson, J.J. Baumberg, G.A.J. Amaratunga, Metamaterial high pass filter based on periodic wire arrays of multiwalled carbon nanotubes. Appl. Phys. Lett. **97**, 163102 (2010)
12. J.W. Goodman, *Introduction to Fourier Optics*, 2nd edn. (McGraw-Hill Companies, New York, 2005), pp. 55–58
13. R.G. Wilson, *Fourier Series and Optical Transform Techniques in Contemporary Optics* (Wiley, New York, 1995)
14. H. Dammann, K. Görtler, High-efficiency in-line multiple imaging by means of multiple phase holograms. Opt. Commun. **3**, 312–315 (1971)
15. M.A. Seldowitz, J.P. Allebach, D.W. Sweeney, Synthesis of digital holograms by direct binary search. Appl. Opt. **26**, 2788–2798 (1987)
16. R.W. Gerchberg, W.O. Saxon, A practical algorithm for the determination of phase from image and diffraction plane pictures. Optik **35**, 237–246 (1972)
17. J.H. Holland, Genetic algorithms. Sci. Am. **267**, 66–72 (1992)
18. A. Thess, R. Lee, P. Nikolaev, H. Dai, P. Petit, J. Robert, R.E. Smalley, Crystalline ropes of metallic carbon nanotubes. Science **273**, 483–487 (1996)
19. S. Iijima, Helical microtubules of graphitic carbon. Nature **354**, 56–58 (1991)
20. K.B.K. Teo, M. Chhowalla, G.A.J. Amaratunga, W.I. Milne, D.G. Hasko, G. Pirio, P. Legagneux, F. Wyczisk, D. Pribat, Uniform patterned growth of carbon nanotubes without surface carbon. Appl. Phys. Lett. **79**, 1534–1536 (2001)
21. W.I. Milne, K.B.K. Teo, M. Chhowalla, G.A.J. Amaratunga, S.B. Lee, D.G. Hasko, H. Ahmed, O. Groening, P. Legagneux, L. Gangloff, J.P. Schnell, G. Pirio, D. Pribat, M. Castignolles, A. Loiseau, V. Semet, V.T. Binh, Electrical and field emission investigation of individual carbon nanotubes from plasma enhanced chemical vapour deposition. Diam. Relat. Mater. **12**, 422–428 (2003)
22. P.J. Collings, M. Hird, *Introduction to Liquid Crystals, Chemisrty and Physics* (Taylor & Francis Group, London, 1998)
23. M.F. Lin, F.L. Shyu, R.B. Chen, Optical properties of well-aligned multiwalled carbon nanotube bundles. Phys. Rev. B **61**, 14114 (2000)

24. J.B. Pendry, A.J. Holden, D.J. Robbins, W.J. Stewart, Low frequency plasmons in thin-wire structures. J. Phys.: Condens. Matter **10**, 4785–4809 (1998)
25. P. Drude, Zur Elektronentheorie der metalle. Ann. Phys. **306**, 566 (1900)
26. P.G. Etchegoin, E.C. Le Ru, M. Meyer, An analytic model for the optical properties of gold. J. Chem. Phys. **125**, 164705 (2006)
27. H. Butt, Q. Dai, R. Rajesekharan, T.D. Wilkinson, G.A.J. Amaratunga, Plasmonic band gaps and waveguide effects in carbon nanotube arrays based metamaterials. ACS Nano **5**, 9138–9143 (2011)
28. Y. Montelongo, H. Butt, T. Butler, G.A.J. Amaratunga, T.D. Wilkinson, Computer generated holograms for carbon nanotube arrays. Nanoscale **5**, 4217–4222 (2013)
29. H. Butt, T. Butler, Y. Montelongo, R. Ranjith, G.A.J. Amaratunga, T.D. Wilkinson, Continuous diffraction patterns from circular arrays of carbon nanotubes'. Appl. Phys. Lett. **101**, 251102 (2012)
30. M.A. Kaliteevski, S. Brand, R.A. Abram, T.F. Krauss, R. De La Rue, P. Millar, Two-dimensional Penrose-tiled photonic quasicrystals: from diffraction pattern to band structure. Nanotechnology **11**, 274 (2000)
31. H. Butt, Y. Montelongo, T. Butler, R. Rajesekharan, Q. Dai, S.G. Shiva-Reddy, G.A. Amaratunga, T.D. Wilkinson, Carbon nanotube based high resolution holograms. Adv. Mater. (2012). doi:10.1002/adma.201202593
32. S.A. Maier, *Plasmonics: Fundamentals and Applications* (Springer, New York, 2007)
33. G.W. Bryant, F.J. Garcia de Abajo, J. Aizpurua, Mapping the plasmon resonances of metallic nanoantennas. Nano Lett. **8**, 631–636 (2008)
34. L. Novotny, Effective wavelength scaling for optical antennas. Phys. Rev. Lett. **98**, 266802 (2007)
35. W. Yu, K. Takahara, T. Konishi, T. Yotsuya, Y. Ichioka, Fabrication of multilevel phase computer-generated hologram elements based on effective medium theory. Appl. Opt. **39**, 3531–3536 (2000)
36. S. Larouche, Y.-J. Tsai, T. Tyler, N.M. Jokerst, D.R. Smith, Infrared metamaterial phase holograms. Nat. Mater. **11**, 450–454 (2012)
37. W. Khunsin, B. Brian, J. Dorfmüller, M. Esslinger, R. Vogelgesang, C. Etrich, C. Rockstuhl, A. Dmitriev, K. Kern, Long-distance indirect excitation of nanoplasmonic resonances. Nano Lett. **11**, 2765–2769 (2011)
38. P. West, S. Ishii, G.V. Naik, N.K. Emani, V.M. Shalaev, A. Boltasseva, Searching for better plasmonic materials. Laser Photonics Rev. **4**, 795–808 (2010)
39. T. Hessler, M. Rossi, R.E. Kunz, M.T. Gale, Analysis and optimization of fabrication of continuous-relief diffractive optical elements. Appl. Opt. **37**, 4069–4079 (1998)
40. K.R. Catchpole, A. Polman, Design principles for particle plasmon enhanced solar cells. Appl. Phys. Lett. **93**, 191113 (2008)